JACS
JOURNAL OF THE AMERICAN CHEMICAL SOCIETY
pubs.acs.org/JACS
Article

Bimetallic Metal Sites in Metal–Organic Frameworks Facilitate the Production of 1-Butene from Electrosynthesized Ethylene

Mi Gyoung Lee,[▽] Sharath Kandambeth,[▽] Xiao-Yan Li,[▽] Osama Shekhah, Adnan Ozden, Joshua Wicks, Pengfei Ou, Sasa Wang, Roham Dorakhan, Sungjin Park, Prashant M. Bhatt, Vinayak S. Kale, David Sinton, Mohamed Eddaoudi,* and Edward H. Sargent*

Cite This: *J. Am. Chem. Soc.* 2024, 146, 14267–14277

Read Online

ACCESS | Metrics & More | Article Recommendations | Supporting Information

ABSTRACT: Converting CO_2 to synthetic hydrocarbon fuels is of increasing interest. In light of progress in electrified CO_2 to ethylene, we explored routes to dimerize to 1-butene, an olefin that can serve as a building block to ethylene longer-chain alkanes. With goal of selective and active dimerization, we investigate a series of metal–organic frameworks having bimetallic catalytic sites. We find that the tunable pore structure enables optimization of selectivity and that periodic pore channels enhance activity. In a tandem system for the conversion of CO_2 to 1-C_4H_8, wherein the outlet cathodic gas from a CO_2-to-C_2H_4 electrolyzer is fed directly (via a dehumidification stage) into the C_2H_4 dimerizer, we study the highest-performing MOF found herein: M′ = Ru and M″ = Ni in the bimetallic two-dimensional $M'_2(OAc)_4M''(CN)_4$ MOF. We report a 1-C_4H_8 production rate of 1.3 mol g_{cat}^{-1} h^{-1} and a C_2H_4 conversion of 97%. From these experimental data, we project an estimated cradle-to-gate carbon intensity of −2.1 kg-CO_2e/kg-1-C_4H_8 when CO_2 is supplied from direct air capture and when the required energy is supplied by electricity having the carbon intensity of wind.

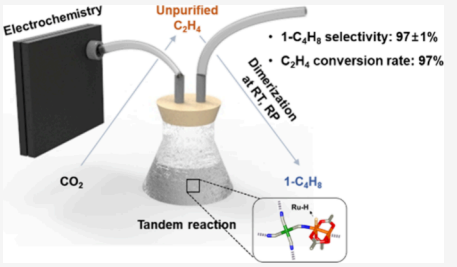

INTRODUCTION

Aviation fuels play a significant role in CO_2 emissions, contributing to about 2.4% of global emissions. The aviation sector is projected to emit approximately 430 Mt of CO_2 in 2050, which, given deep decarbonization forecast in other sectors, could account for as much as 25% of global CO_2 emissions by that year.[1]

These considerations motivate efforts aimed at converting CO_2 (ideally captured from air) to fuels. One avenue is direct 1-butene (1-C_4H_8) production from CO_2; for 1-C_4H_8, it can serve as a precursor to synthetic jet fuel.[2−4] Unfortunately, there are as yet no energy-efficient reports converting CO_2 to 1-C_4H_8 via an electrified route. The electrochemical CO_2 reduction reaction (eCO_2RR) has advanced CO_2 conversion to ethylene, but the conversion of ethylene to 1-C_4H_8 relies on high temperature and pressure (10 to 100 bar),[5−9] potentially curtailing integration with low-temperature electrolyzers.

We considered first why C_2H_4 dimerization fails, in prior reports, to occur efficiently at atmospheric pressure (1 atm) and room temperature (25 °C) (ambient conditions). We posited that the density of active sites may be insufficient for high-activity reaction among C_2H_4 molecules at these pressures and that the absence of confined active sites deteriorates selectivity in dimerization to 1-C_4H_8.[10−13]

With these considerations in mind, we pursued a metal–organic framework (MOF)-based approach, seeking to lever a tunable pore structure to achieve selectivity and to combine this with open porosity (including periodic pore channels) and a high surface area to enhance activity.[14−23] Specifically, we focused on a family of bimetallic two-dimensional (2D) MOFs, $M'_2(OAc)_4M''(CN)_4$ 2D MOF (denoted as H_2:M′M″MOF), which allow the integration of multiple catalytic centers in their periodic structure through defect-engineering, including via thermal treatment.[18] A thermally treated bimetallic 2D MOF with high surface area would offer enhanced exposure of catalytic sites to C_2H_4 molecules at 1 atm of pressure; and periodic pore channels would further improve the diffusion of reactants and selectivity of 1-C_4H_8 during C_2H_4 dimerization reaction.[24,25]

We then prototype CO_2 to 1-C_4H_8, with a CO_2-to-C_2H_4 electrolyzer whose outlet cathodic gas is fed directly (with the aid of dehumidification) into the C_2H_4 dimerizer and where we use the optimal MOF found herein: M′ = Ru and M″ = Ni in H_2:M′M″MOF. We report a 1-C_4H_8 production rate of 1.3 mol g_{cat}^{-1} h^{-1} and a C_2H_4 conversion of 97%. We then estimate, based on these experimental data, the potential for decarbonization compared with existing routes.

Received: March 18, 2024
Revised: April 23, 2024
Accepted: April 24, 2024
Published: May 8, 2024

https://doi.org/10.1021/jacs.4c03806
J. Am. Chem. Soc. 2024, 146, 14267−14277

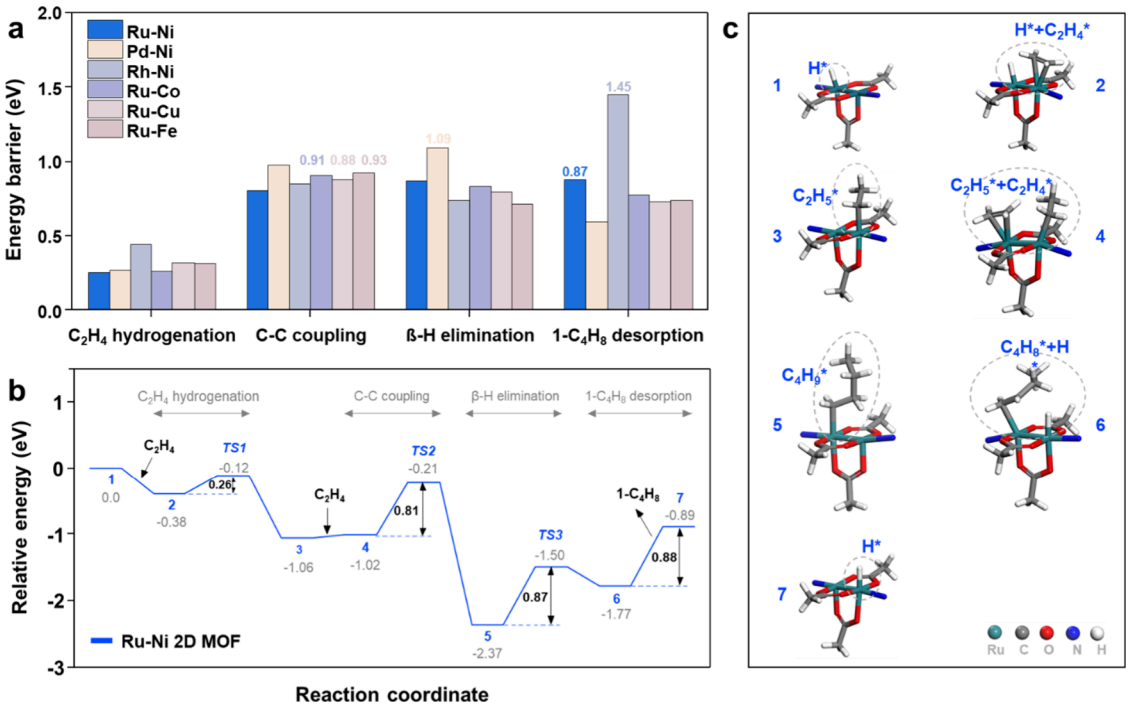

Figure 1. DFT calculation of C_2H_4 dimerization on different combinations of metals ($M'_2(OAc)_4M''(CN)_4$ MOF; M′: Ru, Rh, and Pd; M″: Ni, Co, Cu, and Fe). (a) Energy barriers for four elementary steps of C_2H_4 hydrogenation, C−C coupling, β-H elimination, and 1-C_4H_8 desorption. (b) Complete reaction pathway from C_2H_4 adsorption to the formation of 1-C_4H_8 on the H_2:RuNi MOF. (c) Corresponding geometries of reaction centers.

RESULTS

Computational Screening of $M'_2(OAc)_4M''(CN)_4$ 2D MOF Catalysts. We posited that hydrogen activation on the metal surface could create reactive metal hydride species as intermediates for carbon chain production during C_2H_4 dimerization. We were inspired by such effects in related hydrogenation and Fischer−Tropsch reactions.[21,26] We therefore explored treating the MOF $M'_2(OAc)_4M''(CN)_4$ at elevated temperatures in a H_2 environment, and our goal was to remove the acetoxy group (OAc) and leave behind sufficient porosity for C_2H_4 adsorption and dimerization to 1-C_4H_8. These considerations motivated us to begin with H_2-treated $M'_2(OAc)_4M''(CN)_4$ 2D MOF (denoted as H_2:M′M″MOF), considering the principle of hard and soft acids and bases applied to the construction of stable 2D MOFs.[27]

To pursue high catalytic activity, we began by screening M′ and M″ sites using density functional theory (DFT) calculations, comparing reaction barriers of key elementary steps in the 1-C_4H_8 formation process (details in Experimental Methods). Invoking the Cossee−Arlman[12] mechanism employed in modeling the polymerization of alkenes via the successive insertion of ethylene monomers (Figure S1),[9,12,21,28,29] we considered these four key elementary steps associated with C_2H_4 dimerization into 1-C_4H_8: (1) C_2H_4 hydrogenation ($C_2H_4^* + H^* \rightarrow C_2H_5^*$), (2) C−C coupling ($C_2H_4^* + C_2H_5^* \rightarrow C_4H_9^*$), (3) β-H elimination ($C_4H_9^* \rightarrow C_4H_8^* + H^*$), and (4) 1-$C_4H_8$ desorption ($C_4H_8^* + H^* \rightarrow C_4H_8(g) + H^*$)).[30,31]

We investigated, *in silico*, candidate thermocatalytic reaction pathways (Figure 1), starting from C_2H_4 adsorption and ending with the desorption of 1-C_4H_8, looking at six H_2:M′M″MOF catalyst candidates, where M′ = Ru, Rh, and Pd, and M″ = Ni, Co, Cu, and Fe (Figure S2). We first fixed Ni as the M″ site in the $M''(CN)_4$ connector while varying M′ elements in the $M'_2(OAc)_4$ cluster, since Ni-based MOFs are known to be effective in C_2H_4 dimerization. We then calculated the reaction energies by obtaining transition states for every elementary step of Figure 1a, where the hydrogenation of adsorbed C_2H_4 is relatively easily performed. Among candidates for the M′ site in H_2:M′M″MOF, Ru shows the lowest energy barrier of 0.80 eV for the C−C coupling step to interact in a concerted manner with two ethene molecules. Looking across the full pathway, we observed that the highest energy barriers (considering candidate MOFs Ru−Ni, Pd−Ni, and Rh−Ni) are 0.87 eV for 1-C_4H_8 desorption, 1.09 eV for β-H elimination, and 1.45 eV for 1-C_4H_8 desorption.

We then moved to substituting the M″ sites with Co, Cu, and Fe while keeping Ru fixed at the M′ site. We found that C−C coupling was the rate-determining step for all elemental combinations in H_2:M′M″ MOFs, where the energy barriers are 0.91, 0.88, and 0.93 eV. For 2D $M'_2(OAc)_4M''(CN)_4$ MOFs, two M′ sites in $M'_2(OAc)_4$ clusters play a critical role in optimizing the reaction energy barrier, while the M″ site in the $M''(CN)_4$ connector does not impact the reaction.

We performed additional DFT calculations to investigate whether the M″ site in the bimetallic two-dimensional (2D) MOF of $M'_2(OAc)_4M''(CN)_4$ may serve as an active site, considering three configurations of C_2H_4 adsorption in Figure S3a,b. We observe the spontaneous desorption of C_2H_4, as illustrated in Figure S3d−f. These results indicate that the M″ site with square planar coordination in the 2D $M'_2(OAc)_4M''(CN)_4$ MOF structure is not conducive to C_2H_4 adsorption, providing one piece of evidence against the notion that the M″ site serving as a principal active site for catalyzing C−C dimerization of ethylene results in the production of 1-C_4H_8. H_2:RuNi MOF shows the lowest

https://doi.org/10.1021/jacs.4c03806
J. Am. Chem. Soc. 2024, 146, 14267−14277

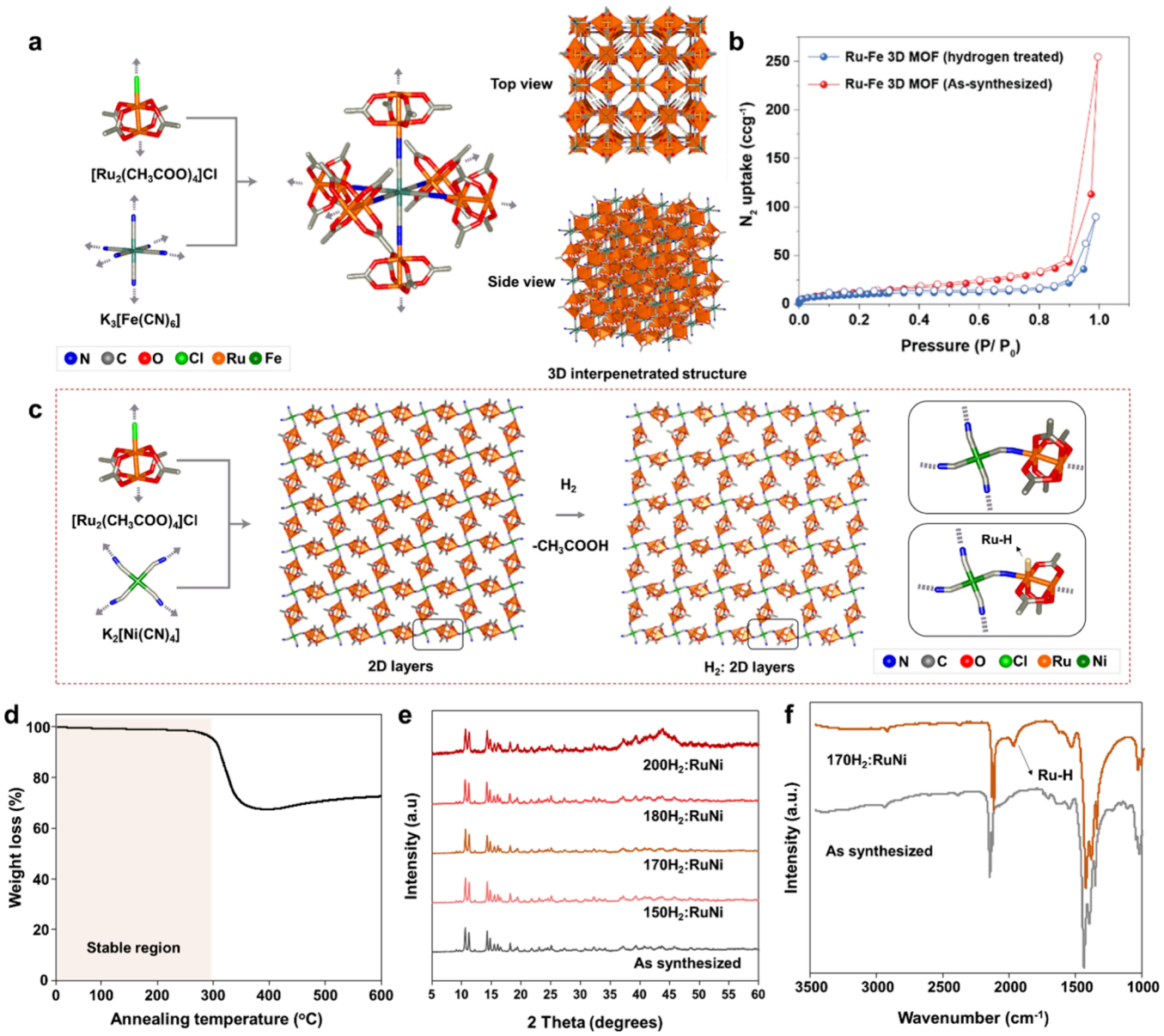

Figure 2. Design and characterization of M′M″ MOF catalysts. (a) Construction of RuFe MOF by the reaction of $K_3[Fe(CN)_6]$ with $Ru_2(CH_3COO)_4Cl$. (b) N_2 uptake of RuFe MOF before and after the H_2 treatment. (c) Structure of RuNi MOF before and after H_2 treatment. (d) TGA profiles and (e) PXRD patterns of H_2:RuNi MOF with different H_2-treated temperatures. (f) FTIR spectra of RuNi MOF and $170H_2$:RuNi MOF.

activation energy for C_2H_4 dimerization to 1-C_4H_8, where Figure 1b plots the full reaction pathway from ethylene adsorption to the generation of 1-C_4H_8.

Ru-clusters in this MOF are the major active site centers; the corresponding atomic configurations of Ru-clusters are shown in Figure 1c.

Synthesis and Characterization of Bimetallic H_2:M′M″MOF Catalysts. We sought to synthesize and study the H_2:M′M″MOF shown in Figure 2 and Figures S3−S6. Experimentally, we identified two distinct types of structures in the reaction of acetate clusters of Ru, in combination with cyano precursors of Fe, Co, and Ni. The combination of octahedral $K_3[Fe(CN)_6]$ and $K_3[Co(CN)_6]$ building units with linear ditopic ruthenium acetate clusters $[Ru_2(OAc)_4]Cl$ resulted in a three-dimensional MOF (3D MOF) structure with interpenetrated pcu topology (Figure 2a and Figure S4).[32]

We found that it is challenging to create, using H_2 treatment, Ru−H species in these interpenetrated 3D MOFs, as evident from the no change in porosity based on the N_2 sorption study, a finding we attribute to their dense nonporous structure (Figure 2b). As in the case of RuFe and RuCo, the tetrahedral geometry of the $Cu(CN)_4$ building blocks hinders the formation of the desired 2D MOF structure, and such a structure has yet to be reported experimentally.

When we reacted ditopic $[Ru_2(OAc)_4]Cl$ with square planar tetratopic $K_2[Ni(CN)_4]$ precursors, we obtained a 2D MOF having the desired sql topology (Figure 2c). We believe that it is the 2D layered architecture of this structure that enabled more efficient reactant diffusion and, thus, the generation of catalytically active Ru−H functionalities upon H_2 treatment. When we sought axially to link $Ru_2(OAc)_4$ with tetra-cyano (CN)-functionalized $[NiCN_4]_2$ building blocks, we obtained

https://doi.org/10.1021/jacs.4c03806
J. Am. Chem. Soc. 2024, 146, 14267−14277

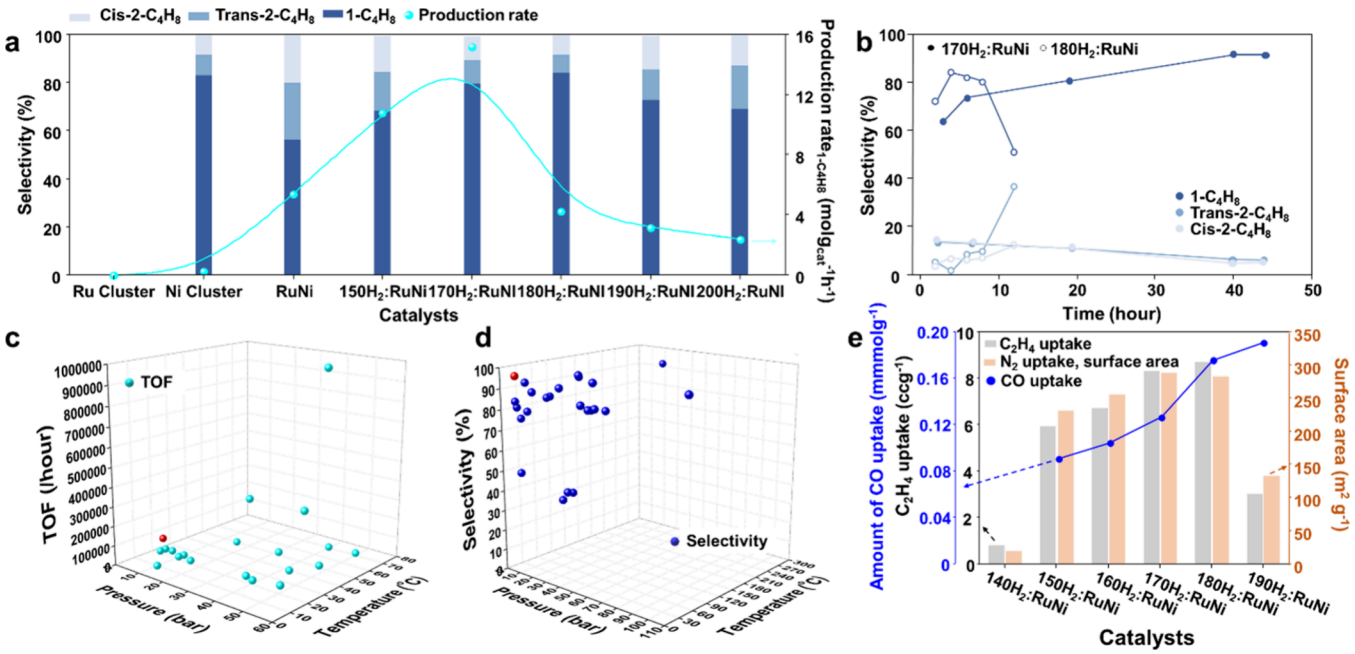

Figure 3. C_2H_4 dimerization performance under ambient conditions and gas uptake study. (a) Selectivity, and production rate of H_2:RuNi MOF at different H_2-treated temperatures. (b) Selectivity comparison between $170H_2$:RuNi MOF and $180H_2$:RuNi MOF. (c) TOF and (d) selectivity (1-C_4H_8) of C_2H_4 dimerization catalysts (Ni- and Ru-containing MOFs and homogeneous catalysts that are commercial catalysts) under different pressure and temperature conditions. Red circles indicate $170H_2$:RuNi MOF. Detailed information is available in Table S2. Twenty-three types of catalysts are compared with H_2:RuNi MOF. Because the TOFs of the four commercial homogeneous catalysts listed in Table S2 (entries 21−24) are low, these four catalysts appear only in the selectivity comparison. (e) Adsorption isotherms of C_2H_4, N_2, and CO for H_2:RuNi MOF at different H_2-treated temperatures.

(PXRD) evidence of the bimetallic RuNi MOF structure (Figure 2d and Experimental Methods).[33]

In light of DFT calculations, we explored the possibility of replacing the Ru precursor with either Rh or Pd precursors (Figure S5). However, in the case of the $(Ru_2(OAc)_4Cl)$ paddle wheel precursor, the cluster has a combination of mixed-valent Ru^{2+} and Ru^{3+} metal ions, allowing negatively charged $[NiCN_4]^{2-}$ and $[Fe(CN)_6]^{3-}$ units to connect axially with the Ru metal ions in the $(Ru_2(OAc)_4)$ cluster.[32] Unfortunately, the mixed-valent cluster of Rh and Pd ($[M_2(OAc)_2Cl]$, where M = Rh and Pd) is not seen. Nevertheless, the reported paddle wheel clusters of $[Rh_2(OAc)_4]$[34] and $[Pd_2(OAc)_4]$ contain metal ions of a single oxidation state, i.e., Rh^{2+} and Pd^{2+}. As a result, experimentally, the axial connection of negatively charged $[NiCN_4]^{2-}$ units to $[Rh_2(OAc)_4]$ or $[Pd_2(OAc)_4]$ clusters and the subsequent 2D MOF construction do not arise. In line with DFT conclusions, RuNi is the only combination among H_2:MM MOFs that forms the targeted 2D MOF structure with accessible porosity following H_2 treatment.

After synthesizing the 2D RuNi MOF, we treated it using H_2 at temperatures ranging from 150 to 200 °C and our goal was to produce the catalytically active (Ru−H) sites for C_2H_4 dimerization by eliminating CH_3COOH (Figure 2c).[21] Post-treatment characterization with thermogravimetric analysis (TGA) and powder X-ray diffraction (PXRD) revealed the high structural stability of the MOF upon H_2 annealing at temperatures up to 200 °C (Figure 2d,e and Figures S6 and S7). This is accounted for by noting that the ruthenium carboxylate linkages (Ru-COO) play no active role in framework construction;[35] as a result, the MOF structure is not altered when the Ru−H catalytic site is formed by cleaving the Ru-COO coordination.

A broad peak was seen in the PXRD pattern of the $200H_2$:RuNi MOF from 40° to 45°, indicating the formation of excessive defects in the $200H_2$:RuNi MOF. The retention of PXRD peaks of RuNi MOF over a range of hydrogen annealing temperatures (from 150 to 200 °C) indicates its high structural stability.

We checked for evidence of structural degradation of RuNi MOF to Ru−Ni nanoparticles during H_2 treatment: the PXRD of H_2:RuNi MOF samples does not show extra diffraction peaks corresponding to other RuNi structures; this is evidenced from the comparison with simulated PXRD patterns.[36−38]

In addition, to identify changes in the function of the RuNi MOFs following H_2 treatment, we conducted SEM-energy dispersive X-ray (EDX) spectroscopy (Figure S8). The EDX measurements show that the nitrogen content of the MOF samples did not decrease but rather increased from 8.6 to 10.9%, while the carbon content decreased from 24.2 to 23.1% following H_2 treatment. This suggests that cleavage of the −CN functional group is not a major occurrence.

Fourier transform infrared (FTIR) spectroscopy was also used to query whether chemical linkages have been formed in the RuNi MOF (Figure 2f and Figure S9). The increase in −C≡N− stretching frequency (2145 cm^{-1}) of RuNi MOF in comparison to that of the $K_2[Ni(CN)_4]$ precursor (2120 cm^{-1}) was ascribed to the complexation of Ru within the $[Ru_2(O_2CMe)_4]Cl$ cluster with the −C≡N− functionalities of $K_2[Ni(CN)_4]$.[39] The generation of catalytically active Ru−H functionalities in RuNi MOF upon H_2 treatment was witnessed via the emergence of a new peak at 1990 cm^{-1} in FTIR spectra following H_2 treatment, indicative of the formation of Ru−H bonds.[21,39]

https://doi.org/10.1021/jacs.4c03806
J. Am. Chem. Soc. 2024, 146, 14267−14277

Scanning and transmission electron microscopies (SEM and TEM) show that the morphology and shape of the H_2:RuNi MOF are similar to those of the pristine RuNi MOF, regardless of the temperature of H_2 treatment (Figures S10−12).

We used X-ray photoelectron spectroscopy (XPS) to investigate further the chemical composition and coordination environment (Figures S13 and S14 and Table S1). This showed the coexistence of Ru, Ni, O, and C. The C 1s spectra overlap with Ru 3d spectra, with peaks at 288.5, 286.4, and 284.8 eV corresponding to O−C═O, C−O, and C═C bonds, respectively.[40,41] The signals at 281.9 and 286.4 eV are assigned to Ru $3d_{5/2}$ and Ru $3d_{3/2}$.[42] Peaks at 463.9, 486.5, 462.7, and 485.2 eV belong to Ru^0 $3p_{3/2}$, Ru^0 $3p_{1/2}$, Ru^{x+} $3p_{3/2}$, and Ru^{x+} $3p_{1/2}$, respectively.[42−44] The Ni 2p spectral features at 856.9 and 875.4 eV are Ni $2p_{3/2}$ and Ni $2p_{1/2}$, respectively, the peaks characteristic of Ni^{2+}. The O 1s spectra were deconvoluted into three peaks with their binding energies at 531.2 eV, 532.0, and 532.8 eV. These peaks are assigned to Ni (Ru)−O, O−C═O, and absorbed water species.[45] The XPS results agree with the expected structure of the H_2:RuNi MOF: Ru-based carboxylate paddle wheel clusters have a mixed valence of Ru (Ru^{2+} and Ru^{3+}) that bridges the CN functionalities of the $[NiCN_4]^{2-}$ complex, which facilitates the formation of extended MOF structures.

C_2H_4 Dimerization under Ambient Conditions. Using gas chromatography equipped with mass chromatography and nuclear magnetic resonance spectroscopy (^{1}H NMR and C NMR), we tracked the selectivity and production rate when we employed $[Ru_2(OAc)_4]Cl$ and $K_2[Ni(CN)_4]$ clusters, the building block components of the MOF and bimetallic RuNi MOF with different Ru−H functionalities (Figure 3a). We observed no measurable >C_4 products (Figure S15). Previous work[46] has similarly reported C_4 products as the most selectively produced ones from C_2H_4 dimerization at near-atmospheric pressure and temperature.

We investigated the catalytic activity of $[Ru_2(OAc)_4]Cl$ and found that it does not provide C_2H_4 dimerization; this was ascribed to the absence of Ru−H functionalities. Conversely, the $Ni(CN)_4$ clusters produced 1-C_4H_8 with 80% selectivity, but the production rate was a low 0.265 mol g_{cat}^{-1} h^{-1}, which we assign to the nonporous nature of the catalyst. From this, we conclude that the square planar Ni unit within $K_2Ni(CN)_4$ may contribute to the C_2H_4 dimerization activity, potentially accounting for the catalytic activity observed in the pristine MOF.

We then assessed the C_2H_4 dimerization performance of RuNi MOF, which showed an improved production rate of 5 mol g_{cat}^{-1} h^{-1}; however, its selectivity values were 56% to 1-C_4H_8, 24% to *trans*-2-C_4H_8, and 20% to *cis*-2-C_4H_8. We note that the absence of Ru−H functionalities and also the limited BET surface area (19 m^2 g^{-1}, Figure S16a) caused the limited selectivity of RuNi MOF.

After H_2 treatment, both the selectivity and production rate of 1-C_4H_8 increased significantly to 84% and 15.2 mol g_{cat}^{-1} h^{-1} (at H_2-treated temperatures of 180 and 170 °C), respectively. We link this to the increase in BET surface area, in addition to the existence of Ru−H functionalities following H_2 treatment, indicative of an increase in porosity and access to active sites, thus enabling reaction with C_2H_4, in line with trends seen in the DFT studies presented above. Treating with H_2 at high temperatures (>190 °C) adversely affected C_2H_4 dimerization activity and selectivity to 1-C_4H_8. This may arise due to a loss of surface area and an increase in structural deformation (PXRD, Figure 2d).

To assess the operating stability of the H_2:RuNi MOF, we monitored the C_2H_4 dimerization reaction using 170H_2:RuNi MOF and 180H_2:RuNi MOF for 40 h (Figure 3b). The 170H_2:RuNi MOF showed a consistent 1-C_4H_8 selectivity of 90% for 40 h (Figure S17a), whereas 180H_2:RuNi MOF was limited to 55% 1-C_4H_8 selectivity for 12 h. A similar deterioration of 1-C_4H_8 selectivity was also detected in the 190H_2:RuNi MOF (Figure S17b). We propose that the loss of porosity at high H_2-treated temperature could have an undesirable influence on 1-C_4H_8 selectivity in long-term stability tests. To study the origins of unstable C_2H_4 dimerization after H_2 treatment higher than 180 °C, we investigated the change in the thickness of the H_2:RuNi MOF particle using atomic force microscopy (AFM) (Figure S18). We found that the thickness of the H_2:RuNi MOF particle catalyst declined from 5 to 1 nm after increasing the H_2-treated temperature from 170 to 180 °C. We offer that blocking the open pores of 180H_2:RuNi MOF leads to poor selectivity and yields into 1-C_4H_8.[47,48]

We conducted a performance analysis of the H_2:RuNi MOF in comparison with previously reported MOFs and homogeneous catalysts for C_2H_4 dimerization. As shown in Figure 3c,d and detailed in Table S2, the selectivity and turnover frequency (TOF) of the 170H_2:RuNi MOF are similar to those of reference catalysts, but this was achieved in the present study under ambient temperature and pressure conditions. On the C_2H_4 dimerization performance of H_2:RuNi MOF, we performed gas uptake studies under carbon monoxide (CO), nitrogen (N_2), and C_2H_4 environments.

To clearly query the formation of defects (i.e., Ru−H functionality) in H_2:RuNi MOF, we used a CO molecular adsorption probe (at 298 K), because the C−O vibrational stretching mode is particularly sensitive to metal coordination and therefore provides information on the nature and characteristics of adsorption sites.[39] The measurement of the CO sorption isotherm revealed the irreversible binding of CO in H_2:RuNi MOF (Figure 3e and Figure S19). This rise in the level of CO uptake suggests that more open metal sites (defects) are generated in the H_2:RuNi MOF as the H_2-treatment temperature increases. We observed the formation of a new FTIR peak at 2088 cm^{-1} after the CO sorption of the H_2:RuNi MOF (Figure S20). This peak is attributed to the Ru-CO bond, which was generated by the interaction of CO with open Ru metal sites.[35]

Gas Uptake Studies to Relate Active Sites and Dimerization Performance. To investigate the effect of catalyst features—Ru−H functionalities, surface area, and C_2H_4 affinity—we also analyzed N_2 and C_2H_4 sorption to measure the surface area and C_2H_4 affinity of H_2:RuNi MOF, respectively (Figure 3e and Figures S16 and S21). While the CO (at 298 K) uptake continued to increase with an increased temperature of the H_2 treatment, N_2 (at 77 K) and C_2H_4 (at 298 K) uptakes reached an optimum value at 170 and 180 °C, respectively, but decreased with a further temperature increase. Of all H_2:RuNi MOFs, 170H_2:RuNi MOF and 180H_2:RuNi MOF displayed the highest C_2H_4 uptake (8.7 cc g^{-1}), associated with a surface area of 287 m^2 g^{-1}. These findings reveal that the simultaneous presence of Ru−H active sites, high C_2H_4 affinity, and highest BET surface area lead to the high selectivity and production rate of the 170H_2:RuNi MOF catalyst.

https://doi.org/10.1021/jacs.4c03806
J. Am. Chem. Soc. 2024, 146, 14267−14277

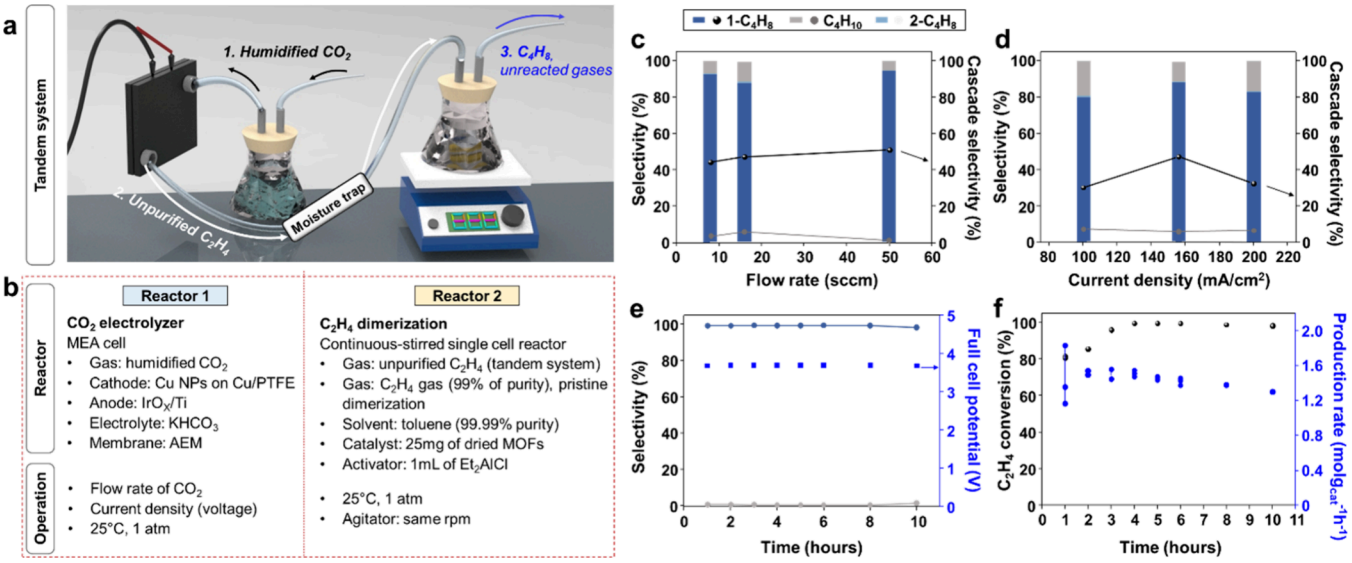

Figure 4. Tandem system implementing eCO_2RR followed by C_2H_4 dimerization. (a) Schematic illustration of the experimental apparatus and device structure. Between the two reactors, a moisture trap is installed. (b) Cell type, components, and operating conditions for two types of reactors: MEA-based CO_2 electrolyzer and continuously stirred single cell reactor. (c) Selectivity and cascade selectivity under different CO_2 flow rates and at a current density of 156 mA/cm^2. (c) Selectivity and cascade selectivity under different current densities at a CO_2 flow rate of 8 sccm. (d) Product distribution and full cell potential for 10 h. (e) C_2H_4 conversion and production rate for 10 h. (f) Comparison of selectivity between fresh and recycled 170H_2:RuNi MOF during 10 h. We performed consistent operations of the cascade system at a constant current density of 156 mA/cm^2 and a constant CO_2 flow rate of 8 sccm.

1-C_4H_8 Synthesis Using C_2H_4 Produced from eCO_2RR. We used a CO_2 electrolyzer to supply C_2H_4 for C_2H_4 dimerization. We built an electrochemical-thermochemical system composed of two units: (1) a membrane electrode assembly (MEA) electrolyzer for the eCO_2RR to C_2H_4 and (2) a dimerization system for thermochemical conversion of C_2H_4 to 1-C_4H_8. We use the term "low-carbon-intensity 1-C_4H_8 production" (Figure 4a,b and Figures S22−S24; details in Experimental Methods) to describe this route, with our premise that electricity could be provided from renewable sources. We define cascade selectivity as the fraction of electrons (which are consumed in the eCO_2RR) that go to the ultimate production of 1-C_4H_8 (detailed in Experimental Methods).

We varied the flow rate of CO_2 in the CO_2-to-1-C_4H_8 system with CO_2 (Figure 4c). It produced three main C_4 products: 88% 1-C_4H_8, 11% C_4H_{10}, and 1% 2-C_4H_8. This corresponds to a cascade selectivity of 47% at 16 sccm of CO_2 and a current density of 156 mA cm^{-2} (Figure 4c,d). We believe that butane (C_4H_{10}) in the product stream, which is atypical compared to prior C_2H_4 dimerization reactions,[49] may arise from humidity in the cascade system. We thus evaluated the operational stability of CO_2 to 1-C_4H_8 when we introduced a moisture trap between the two systems. When we operate at a constant current density of 156 mA cm^{-2}, we observed a 1-C_4H_8 selectivity of 97 ± 1% with a stable full-cell potential of −3.6 ± 0.05 V over 10 h of continuous operation (Figure 4e and Figure S22). The tandem system maintained a 1-C_4H_8 production rate of 1.3 mol g_{cat}^{-1} h^{-1} and a C_2H_4 conversion of 97% for 10 h (Figure 4f).

We assessed the reusability of the H_2:RuNi MOF and found that the recycled catalyst recovered 80% of C_2H_4 dimerization activity compared to a fresh catalyst after 10 h of reaction (Figure S25). XPS measurements revealed that the chemical state and functional groups of the H_2:RuNi MOF remain intact (Figure S26).

We estimated the energy intensity and cradle-to-gate carbon footprint of 1-C_4H_8 production with assumptions appropriate for a technology-readiness level (TRL) of 2[50,51] (Figure 5).

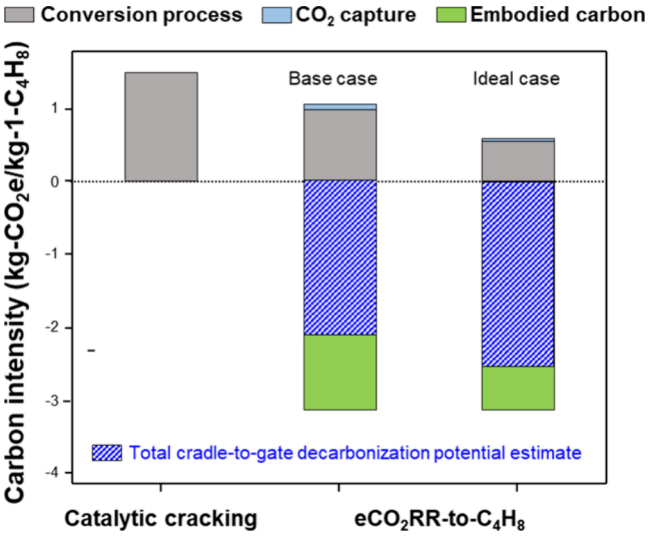

Figure 5. Carbon footprint for 1-C_4H_8 production. For electrochemical processes, we considered renewable wind electricity with a carbon footprint of ∼7 g-CO_2eq/kWh[51] (details are provided in Table S4). Reproduced from ref 51 with permission from the Royal Society of Chemistry. Available under CC-BY 3.0. Copyright [2020] [Royal Society of Chemistry].

The CO_2-to-1-C_4H_8 system required 386 GJ to produce one tonne of 1-C_4H_8 under base conditions (Table S3). The cradle-to-gate decarbonization potential of the process discussed herein using this base condition set (considering the carbon intensity of Ru production) is estimated to be −2.1 kg-CO_2e/kg-1-C_4H_8 when assuming an electricity carbon

https://doi.org/10.1021/jacs.4c03806
J. Am. Chem. Soc. 2024, 146, 14267−14277

intensity of ~7 g-CO_2e/kWh (wind)[52] and CO_2 supplied by direct air capture (Table S4).

DISCUSSION

We synthesized bimetallic H_2:RuNi MOF catalyst and studied their activity of C_2H_4 dimerization to 1-C_4H_8, which is a precursor of SAF. Through a cascade electrochemical-thermochemical system, 1-C_4H_8 was directly produced from CO_2 under ambient conditions, achieving an impressive. These outcomes were made possible by leveraging the synergistic effects of Ru−H and open metal sites within the MOF structure. This cascade route represents the strategic path for generating renewable fuel, ultimately realizing the goal of attaining net-zero carbon emissions in aviation. It serves as a pivotal element in shaping a future global aviation sector that operates with zero-carbon impact.

EXPERIMENTAL METHODS

DFT Calculations. All spin-polarized density functional theory (DFT) calculations were performed by employing the projector-augmented wave method (PAW) as implemented in the Vienna Ab initio Simulation Package (VASP). The generalized gradient approximation in the parametrization of Perdew−Burke−Ernzerhof was implemented to describe the exchange-correlation functional (GGA-PBE). A plane-wave cutoff of 450 eV and 3 × 4 × 3 *k*-point grids generated by the Monkhorst−Pack scheme were used for all the calculations. The zero damping DFT-D3 correction was employed to capture long-range dispersion interactions. For the structural optimization, the electronic self-consistent energy and force were converged to 10^{-6} eV and 0.01 eV/Å, respectively. The constructed atomic models are described as below. For a series of reactions for ethylene dimerization to 1-C_4H_8 formation, we used, by applying the VASP-VTST tool, the climbing image nudged elastic band (CI-NEB) method to search possible transition states for each elementary step. The $M'_2(OAc)_4M''(CN)_4$ MOFs (M′M″ MOFs) were constructed to screen the best combination of M and M″ (for the C_2H_4 dimerization to 1-C_4H_8, where M′ = Ru, Pd, and Rh, and M″ = Ni, Co, Fe, and Cu) (Figure S3). Considering the H_2 treatment, all MOF systems removed a (OAc) that is −CH_3COOH to provide an energy space for C_2H_4 adsorption and dimerization to 1-C_4H_8. The complete reaction pathways for six MOF catalysts were calculated based on the previous Cossee−Arlman mechanism (Figure S1). The four key elementary steps are shown as follows.

C_2H_4 hydrogenation: $C_2H_4^* + H^* \rightarrow C_2H_5^*$

C − C coupling: $C_2H_4^* + C_2H_5^* \rightarrow C_4H_9^*$

β-H elimination: $C_4H_9^* \rightarrow C_4H_8^* + H^*$

1-C_4H_8 desorption: $C_4H_8^* + H^* \rightarrow C_4H_8(g) + H^*$

All atomic configurations are shown in Figure S2, which include all the adsorption intermediates and transition states in reaction per MOF catalyst system.

Synthesis of Tetra-*μ*-acetato-di Ruthenium(II, III) Chloride ($[Ru_2(CH_3COO)_4]Cl$). The $[Ru_2(O_2CMe)_4]Cl$ cluster was prepared by a reported procedure in the literature.[52] Briefly, 1 g of ruthenium chloride hydrate ($RuCl_3 \cdot xH_2O$) and 1 g of anhydrous lithium chloride (LiCl) were refluxed in a mixture of glacial acetic acid (35 mL) and acetic anhydride mixture (7 mL) overnight. The reaction mixture was agitated by constant bubbling of slow stream of oxygen during reflux. The reaction mixture was then cooled, and the red precipitate was collected by centrifugation. After washing with methanol and hexane, the precipitate was dried under vacuum.

Synthesis of RuNi MOF. A stock solution of 150 mg (0.58 mmol) of $K_2[Ni(CN)_4]$ in 30 mL of water and 549 mg (1.15 mmol) of $[Ru_2(CH_3COO)_4]Cl$ in 450 mL of methanol was initially prepared. A $K_2[Ni(CN)_4]$ stock solution was added dropwise to the $[Ru_2(CH_3COO)_4]Cl$ methanol solution in a 1 L round-bottom flask at room temperature. The reaction mixture was then stirred for 4 h. After the orange-brown color was obtained, the precipitate was collected by centrifugation. The precipitate was then repeatedly washed with water and methanol and then dried under vacuum (yield: 85%). The resulting $Ru_2(OAc)_4Ni(CN)_4$ MOF (denoted by RuNi MOF) is constructed from Ru-CN-Ni coordination linkages, which make up the entire MOF structure.

H_2 Treatment of RuNi-Based MOF. H_2 treatment of RuNi MOF was performed on an Autochem II 2920 machine (Micromeritics). The MOF powders were loaded in a quartz U tube sandwiched between two quartz wools. The quartz U tube was then connected to a gas line, which is connected to a furnace. The MOF samples were initially activated by heating at 150 °C under helium gas flow (50 mL/min) for 1 h to remove the solvent and other adsorbed gas impurities. After this activation, MOF samples were subjected to H_2 treatment at different temperatures, ranging from 150 to 200 °C, under a constant flow of H_2 (50 mL/min) and helium (50 mL/min) mixture for 1 h.

Characterization of Catalysts. The morphology of the H_2:RuNi MOF and Cu catalyst was characterized by field emission scanning electron microscopy (SEM, Hitachi SU5000, MERLIN Compact, JEISS) and transmission electron microscopy (TEM). Powder X-ray diffraction (PXRD) patterns were collected using a Bruker D8 ADVANCE diffractometer using a Cu K*α* radiation source (at 40 kV and 40 mA). Surface composition was analyzed with X-ray photoelectron spectroscopy (XPS, Thermo Fisher Scientific K-Alpha) using Al K*α* X-ray radiation. XPS spectra were calibrated with the C 1s peak at 284.5 eV. Fourier-transform infrared spectroscopy (FTIR, ThermoFisher Scientific Nicolet iS50) was conducted to analyze the chemical state and functional groups of Ru and O for the RuNi MOF.

Adsorption Isotherms of N_2, C_2H_4, and CO. Gas adsorption measurements were made using a Micromeritics 3-Flex Surface Characterization Analyzer with increased corrosion resistance (ECR). Liquid nitrogen baths at 77 K were used to regulate the cryogenic temperatures during N_2 adsorption measurements. A thermostat bath set at 298 K was used to regulate the ambient temperature for the adsorption studies of CO and C_2H_4. To prevent any exposure to CO, CO adsorption measurements were performed in a ventilated cage. As a preventative measure, appropriate STANDGAS sensors were employed.

Gas Diffusion Electrodes for CO_2RR. The gas diffusion electrodes for the carbon dioxide reduction reaction (CO_2RR) were prepared by spray-coating a catalyst ink onto a polytetrafluoroethylene (PTFE) substrate (Cu/PTFE). Cu/PTFE was prepared by sputtering Cu onto a hydrophobic PTFE substrate (450 nm average pore size) using pure Cu target (99.999%) in an Angstrom Nexdep sputtering tool at a base pressure of 10^{-6}. Sputtering was conducted with a constant sputtering rate of 0.80 Å/s until a catalyst thickness of approximately 200 nm. For a typical electrode geometric area of 5 cm^2, the catalyst ink was prepared by adding 80 mL of a polymeric binder (Nafion 1100W, perfluorinated resin solution, 5 wt % in mixture of lower aliphatic alcohols and water, containing 45% water) to the ink containing 20 mg of Cu NPs (Sigma-Aldrich, 25 nm particle size (TEM), 99.5%) and 10 mL of isopropanol (Sigma-Aldrich). The resulting ink was then continuously sonicated for 1 h in an ultrasonic bath and spray-coated onto Cu/PTFE until a final catalyst loading of 1.0 mg/cm^2 was achieved. Nominal catalyst loading was ensured by monitoring the weight difference during catalyst deposition. The resulting gas diffusion electrode was then vacuum-dried for 12 h before performing eCO_2RR. Note that an excess amount of catalyst ink was prepared by considering the materials loss during spray deposition. The crystal structure and morphology are shown in Figures S18 and S19.

C_2H_4 Dimerization. The C_2H_4 dimerization activities over the M′M″ MOF catalysts were evaluated in a continuously stirred single cell reactor with an agitator. Typically, 25 mg of catalyst was dissolved in 200 mL of toluene (suitable for HPLC, 99.9%, Sigma-Aldrich).

https://doi.org/10.1021/jacs.4c03806
J. Am. Chem. Soc. 2024, 146, 14267−14277

Before adding the catalysts into toluene, it was dried under vacuum condition and 80 °C. Prior to detection of the product, the M′M″ MOF catalysts were reacted under the ambient conditions (25 °C and 1 atm) for 1 h and a feed (humidified C_2H_4 to mimic the condition of the CO_2 electrolyzer) flow rate of 30 sccm. In these works, C_2H_4 dimerization was typically processed with an addition of 1 mL of activator such as diethylaluminum chloride (Et_2AlCl), which promoted C_2H_4 dimerization without changing the reaction mechanism. Experimentally, we confirmed that there is no other side reaction to generate C_4 products during the C_2H_4 dimerization process on M′M″ MOF catalysts. The effluent gas products of C_2H_4 dimerization reaction were collected 3 times in 1 mL volumes with frequent time intervals and analyzed using gas chromatography−mass spectroscopy (GC-MS) equipped with a detector of FID (column: Rt-Alumina, BOND/KCl PLOT, 30m, 0.32 mm ID, 5.00 um) and nuclear magnetic resonance spectroscopy (^{1}H NMR and C NMR), which were used for the analysis of C_1−C_4 and products with higher carbon number, respectively.

Efficiencies for the C_2H_4 Dimerization Reaction. Dimerization selectivity was defined using eq 1. Dimerization selectivity represents the ratio between a specific product and all of the products.

$$\text{selectivity (\%)} = \frac{\text{moles of carbon in } a \text{ specific group of products (1-}C_4H_8\text{)}}{\text{moles of carbon in the overall detected hydrocarbons}} \times 100 \quad (1)$$

C_2H_4 conversion into C_4 hydrocarbons was calculated using eq 2.

$$C_2H_4 \text{ conversion (\%)} = \frac{\text{molar flow rate of } C_2H_4 \text{ in} - \text{molar flow rate of } C_2H_4 \text{ out}}{\text{molar flow rate of } C_2H_4 \text{ in}} \times 100 \quad (2)$$

Turnover frequency (TOF) was calculated using eq 3.

$$\text{TOF } (h^{-1}) = (\text{number of ethylene consumed})/(\text{catalytic active site} \times \text{time (h)}) \quad (3)$$

eCO_2RR in Neutral Media. The eCO_2RR experiments were conducted in a membrane electrode assembly (MEA) using a neutral media anolyte. Performance testing was conducted via an electrochemical test station. The test station was equipped with a commercial MEA electrolyzer (Dioxide Materials), a current booster (Metrohm Autolab, 10 A), a mass flow controller (Sierra, SmartTrak 100), a humidifier, an electrolyte container, and a peristaltic pump with silicon tubing. The MEA setup was composed of a titanium anode and stainless-steel cathode flow-field plates, both with geometric flow-field areas of 5 cm^2. The MEA was assembled using three components: a cathode electrode (Cu NPs on Cu/PTFE), an anode electrode (IrO_x supported on a titanium (Ti) felt (Fuel Cell Store)), and an anion exchange membrane (AEM, Sustainion X37-50). The cathode electrode was taped onto a stainless-steel plate by using a Cu tape frame, which was then covered by a Kapton tape. The cathode electrode was physically separated from the anode electrode using an AEM in between. The AEM was rinsed with DI water for 10 min prior to the cell assembly. The MEA was then assembled by applying a compression torque to the each of associated bolts. The cathode and anode flow field plates were equipped with flow channels having a serpentine configuration. The cathode flow field was responsible for the continuous supply of humidified CO_2 over the backside of the cathode gas diffusion electrode, whereas the anode flow field was responsible for the continuous supply of the anolyte through the anode electrode. The IrO_x-Ti electrode was prepared using a procedure that involves (1) dipping the Ti felts into an ink containing 2-propanol, iridium(IV) chloride dehydrate (Premion, 99.99%, metal basis, Ir 73%, Alfa Aesar), and hydrochloric acid (HCl), (2) drying for 10 min at 100 °C and sintering for 10 min at 500 °C, and (3) repeating the first two steps until a final Ir mass loading of 1 mg/cm^2 was achieved. Upon completion of the electrolyzer assembly, the anolyte (0.1 M $KHCO_3$) was continuously supplied to the anode chamber with a constant flow rate of 10 mL min^{-1}, and the humidified CO_2 was supplied to the cathode with a constant flow rate of 8 sccm. A constant current density of 100 mA cm^{-2} was applied to initiate the eCO_2RR, and then the current density was gradually increased with 50 mA cm^{-2} increments. The current increments were made upon complete stabilization of the cell potential, typically requiring 30−40 min. For each current density, gas products of CO_2RR were collected 3 times in 1 mL volumes with frequent time intervals and analyzed using gas chromatography (GC). The liquid products of the CO_2RR were collected from both the cathodic and anodic downstream. CO_2RR operation was performed under the current density, enabling the highest FE toward CO_2RR products and, hence, the lowest FE toward hydrogen evolution reaction (HER).e

eCO_2RR Product Analysis. The GC spectra obtained from each gas injection were used to calculate the Faradaic efficiency toward each gas product as follows (eq 4).

$$\text{Faradaic efficiency (\%)} = N \times F \times v \times r/(i \times V_m) \quad (4)$$

where N is the number of electrons transferred, F is the Faradaic constant, v is the gas flow rate at the cathodic downstream, r is the concentration of product(s) in ppm, i is the total current, and V_m is the unit molar volume of product(s). The gas flow rate at the cathodic downstream was measured using a bubble flow meter before collecting the gas samples via gastight syringes. The liquid products of CO_2RR were analyzed by using ^{1}H NMR spectroscopy (600 MHz Agilent DD2 NMR Spectrometer) with water suppression. Dimethyl sulfoxide (DMSO) was used as the reference standard, and deuterium oxide (D_2O) was used as the lock solvent. The NMR spectra obtained at each current density were used to calculate the Faradaic efficiency toward liquid products of CO_2RR as follows (eq 5).

$$\text{Faradaic efficiency (\%)} = N \times F \times n_{\text{product}}/Q \quad (5)$$

where N is the number of electrons transferred, F is the Faradaic constant, n_{product} is the total mole of product(s), and $Q = i \times t$ is the total charge passing through the liquid product collection.

Efficiency for the Cascade eCO_2-to-C_4 System. Cascade selectivity (CO_2-to-C_2H_4-to-C_4H_8) was calculated by using eq 6.

$$\text{cascade selectivity (\%)} = FE_{C2H4}\text{ (\%)} \times C_2H_4 \text{ conversion (\%)} \times \text{dimerization selectivity (\%)} \quad (6)$$

The cascade production rate (mol g_{cat}^{-1} h^{-1}) was calculated using eq 7.

$$\text{cascade production rate (mol } g_{cat}^{-1}\ h^{-1}) = \text{produced amounts of 1 - } C_4H_8 \div \text{catalyst mass (mg)} \div \text{reaction time (h)} \quad (7)$$

■ ASSOCIATED CONTENT

Supporting Information

The Supporting Information is available free of charge at https://pubs.acs.org/doi/10.1021/jacs.4c03806.

Additional DFT calculations, characterization, gas uptakes, electrochemical results, TEA, LCA, and supporting results (PDF)

■ AUTHOR INFORMATION

Corresponding Authors

Mohamed Eddaoudi − *Functional Materials Design, Discovery, and Development (FMD3) research group, Advanced Membranes and Porous Materials (AMPM), Division of Physical Sciences and Engineering, King Abdullah*

https://doi.org/10.1021/jacs.4c03806
J. Am. Chem. Soc. 2024, 146, 14267−14277

University of Science and Technology (KAUST), Thuwal 23955-6900, Kingdom of Saudi Arabia; orcid.org/0000-0003-1916-9837; Email: mohamed.eddaoudi@kaust.edu.sa

Edward H. Sargent − *Department of Electrical and Computer Engineering, University of Toronto, Toronto, ON M5S 1A4, Canada; Department of Chemistry and Department of Electrical and Computer Engineering, Northwestern University, Evanston, Illinois 60208, United States;* orcid.org/0000-0003-0396-6495; Email: ted.sargent@utoronto.ca

Authors

Mi Gyoung Lee − *Department of Electrical and Computer Engineering, University of Toronto, Toronto, ON M5S 1A4, Canada; Department of Materials Science and Engineering, Incheon National University, Incheon 22012, Republic of Korea;* orcid.org/0009-0008-4007-4270

Sharath Kandambeth − *Functional Materials Design, Discovery, and Development (FMD3) research group, Advanced Membranes and Porous Materials (AMPM), Division of Physical Sciences and Engineering, King Abdullah University of Science and Technology (KAUST), Thuwal 23955-6900, Kingdom of Saudi Arabia*

Xiao-Yan Li − *Department of Electrical and Computer Engineering, University of Toronto, Toronto, ON M5S 1A4, Canada; Department of Chemistry, Northwestern University, Evanston, Illinois 60208, United States;* orcid.org/0009-0003-2325-7538

Osama Shekhah − *Functional Materials Design, Discovery, and Development (FMD3) research group, Advanced Membranes and Porous Materials (AMPM), Division of Physical Sciences and Engineering, King Abdullah University of Science and Technology (KAUST), Thuwal 23955-6900, Kingdom of Saudi Arabia;* orcid.org/0000-0003-1861-9226

Adnan Ozden − *Department of Mechanical and Industrial Engineering, University of Toronto, Toronto, ON M5S 3G8, Canada;* orcid.org/0000-0002-6924-1967

Joshua Wicks − *Department of Electrical and Computer Engineering, University of Toronto, Toronto, ON M5S 1A4, Canada;* orcid.org/0000-0001-7819-1167

Pengfei Ou − *Department of Electrical and Computer Engineering, University of Toronto, Toronto, ON M5S 1A4, Canada; Department of Chemistry, Northwestern University, Evanston, Illinois 60208, United States;* orcid.org/0000-0002-3630-0385

Sasa Wang − *Department of Electrical and Computer Engineering, University of Toronto, Toronto, ON M5S 1A4, Canada*

Roham Dorakhan − *Department of Electrical and Computer Engineering, University of Toronto, Toronto, ON M5S 1A4, Canada;* orcid.org/0000-0001-8104-7174

Sungjin Park − *Department of Electrical and Computer Engineering, University of Toronto, Toronto, ON M5S 1A4, Canada*

Prashant M. Bhatt − *Functional Materials Design, Discovery, and Development (FMD3) research group, Advanced Membranes and Porous Materials (AMPM), Division of Physical Sciences and Engineering, King Abdullah University of Science and Technology (KAUST), Thuwal 23955-6900, Kingdom of Saudi Arabia*

Vinayak S. Kale − *Functional Materials Design, Discovery, and Development (FMD3) research group, Advanced Membranes and Porous Materials (AMPM), Division of Physical Sciences and Engineering, King Abdullah University of Science and Technology (KAUST), Thuwal 23955-6900, Kingdom of Saudi Arabia;* orcid.org/0000-0001-7869-0660

David Sinton − *Department of Mechanical and Industrial Engineering, University of Toronto, Toronto, ON M5S 3G8, Canada;* orcid.org/0000-0003-2714-6408

Complete contact information is available at: https://pubs.acs.org/10.1021/jacs.4c03806

Author Contributions

[▽]M.G.L., S.K., and X.-Y.L. contributed equally to this work.

Notes

The authors declare no competing financial interest.

■ ACKNOWLEDGMENTS

All DFT calculations were performed on the Niagara supercomputer of the SciNet HPC Consortium. SciNet is funded by the Canada Foundation for Innovation, the Government of Ontario, Ontario Research Fund Research Excellence Program, and the University of Toronto. M.G.L. is supported by a research grant (2023-0387) from Incheon National University.

■ REFERENCES

(1) Graver, B.; Zhang, K.; Rutherford, D. CO_2 emissions from commercial aviation:2013, 2018 and 2019, In *International Council on Clean Transportation*; International Council on Clean Transportation 2020.

(2) Geleynse, S.; Brandt, K.; Garcia-Perez, M.; Wolcott, M.; Zhang, X. The alcohol-to-jet conversion pathway for drop-in biofuels: techno-economic evaluation. *ChemSusChem* **2018**, *11* (21), 3728−3741.

(3) Silva Braz, D.; Pinto Mariano, A. Jet fuel production in eucalyptus pulp mills: Economics and carbon footprint of ethanol vs. butanol pathway. *Bioresour. Technol.* **2018**, *268*, 9−19.

(4) Kim, H.; Kim, D.; Park, Y.-K.; Jeon, J.-K. Synthesis of jet fuel through the oligomerization of butenes on zeolite catalysts. *Res. Chem. Intermed.* **2018**, *44*, 3823−3833.

(5) Finiels, A.; Fajula, F.; Hulea, V. Nickel-based solid catalysts for ethylene oligomerization−a review. *Catal. Sci. Technol.* **2014**, *4* (8), 2412−2426.

(6) Attanatho, L.; Lao-ubol, S.; Suemanotham, A.; Prasongthum, N.; Khowattana, P.; Laosombut, T.; Duangwongsa, N.; Larpkiattaworn, S.; Thanmongkhon, Y. Jet fuel range hydrocarbon synthesis through ethylene oligomerization over platelet Ni-AlSBA-15 catalyst. *SN Appl. Sci.* **2020**, *2*, 1−12.

(7) Bryliakov, K. P.; Antonov, A. A. Recent progress of transition metal based catalysts for the selective dimerization of ethylene. *J. Organomet. Chem.* **2018**, *867*, 55−61.

(8) Boulens, P.; Pellier, E.; Jeanneau, E.; Reek, J. N.; Olivier-Bourbigou, H.; Breuil, P.-A. R. Self-assembled organometallic nickel complexes as catalysts for selective dimerization of ethylene into 1-butene. *Organometallics* **2015**, *34* (7), 1139−1142.

(9) Chen, C.; Alalouni, M. R.; Dong, X.; Cao, Z.; Cheng, Q.; Zheng, L.; Meng, L.; Guan, C.; Liu, L.; Abou-Hamad, E.; Wang, J.; Shi, Z.; Huang, K. W.; Cavallo, L.; Han, Y. Highly active heterogeneous catalyst for ethylene dimerization prepared by selectively doping Ni on the surface of a zeolitic imidazolate framework. *J. Am. Chem. Soc.* **2021**, *143* (18), 7144−7153.

(10) Mancuso, J. L.; Gaggioli, C. A.; Gagliardi, L.; Hendon, C. H. Singlet-to-triplet spin transitions facilitate selective 1-butene formation during ethylene dimerization in Ni (II)-MFU-4 l. *J. Phys. Chem. C* **2021**, *125* (40), 22036−22043.

(11) Liu, P.; Redekop, E.; Gao, X.; Liu, W.-C.; Olsbye, U.; Somorjai, G. A. Oligomerization of light olefins catalyzed by brønsted-acidic metal−organic framework-808. *J. Am. Chem. Soc.* **2019**, *141* (29), 11557−11564.
(12) Kong, F.; Ríos, P.; Hauck, C.; Fernández-de-Córdova, F. J.; Dickie, D. A.; Habgood, L. G.; Rodríguez, A.; Gunnoe, T. B. Ethylene dimerization and oligomerization using bis (phosphino) boryl supported Ni complexes. *J. Am. Chem. Soc.* **2023**, *145* (1), 179−193.
(13) Joshi, R.; Zhang, G.; Miller, J. T.; Gounder, R. Evidence for the coordination−insertion mechanism of ethene dimerization at nickel cations exchanged onto beta molecular sieves. *ACS. Catal.* **2018**, *8* (12), 11407−11422.
(14) Canivet, J.; Aguado, S.; Schuurman, Y.; Farrusseng, D. MOF-supported selective ethylene dimerization single-site catalysts through one-pot postsynthetic modification. *J. Am. Chem. Soc.* **2013**, *135* (11), 4195−4198.
(15) Freund, R.; Zaremba, O.; Arnauts, G.; Ameloot, R.; Skorupskii, G.; Dincă, M.; Bavykina, A.; Gascon, J.; Ejsmont, A.; Goscianska, J.; Kalmutzki, M.; Lächelt, U.; Ploetz, E.; Diercks, C. S.; Wuttke, S. The current status of MOF and COF applications. *Angew. Chem., Int. Ed.* **2021**, *60* (45), 23975−24001.
(16) Metzger, E. D.; Comito, R. J.; Wu, Z.; Zhang, G.; Dubey, R. C.; Xu, W.; Miller, J. T.; Dincă, M. Highly selective heterogeneous ethylene dimerization with a scalable and chemically robust MOF catalyst. *ACS Sustain. Chem. Eng.* **2019**, *7* (7), 6654−6661.
(17) Metzger, E. D.; Brozek, C. K.; Comito, R. J.; Dincă, M. Selective dimerization of ethylene to 1-butene with a porous catalyst. *ACS Cent. Sci.* **2016**, *2* (3), 148−153.
(18) Fang, Z.; Bueken, B.; De Vos, D. E.; Fischer, R. A. Defect-engineered metal−organic frameworks. *Angew. Chem., Int. Ed.* **2015**, *54* (25), 7234−7254.
(19) Hu, Y.; Zhang, Y.; Han, Y.; Sheng, D.; Shan, D.; Liu, X.; Cheng, A. Ultrathin nickel-based metal−organic framework nanosheets as reusable heterogeneous catalyst for ethylene dimerization. *ACS Appl. Nano Mater.* **2019**, *2* (1), 136−142.
(20) Wang, X.-N.; Zhang, P.; Kirchon, A.; Li, J.-L.; Chen, W.-M.; Zhao, Y.-M.; Li, B.; Zhou, H.-C. Crystallographic visualization of postsynthetic nickel clusters into metal−organic framework. *J. Am. Chem. Soc.* **2019**, *141* (34), 13654−13663.
(21) Agirrezabal-Telleria, I.; Luz, I.; Ortuño, M. A.; Oregui-Bengoechea, M.; Gandarias, I.; López, N.; Lail, M. A.; Soukri, M. Gas reactions under intrapore condensation regime within tailored metal−organic framework catalysts. *Nat. Commun.* **2019**, *10* (1), 2076.
(22) Liu, J.; Ye, J.; Li, Z.; Otake, K. i.; Liao, Y.; Peters, A. W.; Noh, H.; Truhlar, D. G.; Gagliardi, L.; Cramer, C. J.; Farha, O. K.; Hupp, J. T. Beyond the active site: tuning the activity and selectivity of a metal−organic framework-supported Ni catalyst for ethylene dimerization. *J. Am. Chem. Soc.* **2018**, *140* (36), 11174−11178.
(23) Madrahimov, S. T.; Gallagher, J. R.; Zhang, G.; Meinhart, Z.; Garibay, S. J.; Delferro, M.; Miller, J. T.; Farha, O. K.; Hupp, J. T.; Nguyen, S. T. Gas-phase dimerization of ethylene under mild conditions catalyzed by MOF materials containing (bpy) NiII complexes. *ACS. Catal.* **2015**, *5* (11), 6713−6718.
(24) Hou, X.; Wang, J.; Mousavi, B.; Klomkliang, N.; Chaemchuen, S. Strategies for induced defects in metal−organic frameworks for enhancing adsorption and catalytic performance. *Dalton Trans.* **2022**, *51* (21), 8133−8159.
(25) Heinz, W. R.; Junk, R.; Agirrezabal-Telleria, I.; Bueken, B.; Bunzen, H.; Gölz, T.; Cokoja, M.; De Vos, D.; Fischer, R. A. Thermal defect engineering of precious group metal−organic frameworks: impact on the catalytic cyclopropanation reaction. *Catal. Sci. Technol.* **2020**, *10* (23), 8077−8085.
(26) Parr, J. M.; Crimmin, M. R. Carbon-carbon bond formation from carbon monoxide and hydride: the role of metal formyl intermediates. *Angew. Chem., Int. Ed.* **2023**, *135* (19), No. e202219203.
(27) Hamisu, A. M.; Ariffin, A.; Wibowo, A. C. Cation exchange in metal-organic frameworks (MOFs): The hard-soft acid-base (HSAB) principle appraisal. *Inorg. Chim. Acta* **2020**, *511*, No. 119801.
(28) LiBretto, N. J.; Xu, Y.; Quigley, A.; Edwards, E.; Nargund, R.; Vega-Vila, J. C.; Caulkins, R.; Saxena, A.; Gounder, R.; Greeley, J.; Zhang, G.; Miller, J. T. Olefin oligomerization by main group Ga^{3}+ and Zn^{2+} single site catalysts on SiO_2. *Nat. Commun.* **2021**, *12* (1), 2322.
(29) Robinson, R., Jr; McGuinness, D. S.; Yates, B. F. The mechanism of ethylene dimerization with the Ti (OR′) 4/AlR3 catalytic system: DFT studies comparing metallacycle and Cossee proposals. *ACS. Catal.* **2013**, *3* (12), 3006−3015.
(30) Ye, J.; Gagliardi, L.; Cramer, C. J.; Truhlar, D. G. Computational screening of MOF-supported transition metal catalysts for activity and selectivity in ethylene dimerization. *J. Catal.* **2018**, *360*, 160−167.
(31) Pellizzeri, S.; Barona, M.; Bernales, V.; Miró, P.; Liao, P.; Gagliardi, L.; Snurr, R. Q.; Getman, R. B. Catalytic descriptors and electronic properties of single-site catalysts for ethene dimerization to 1-butene. *Catal. Today* **2018**, *312*, 149−157.
(32) Vos, T. E.; Liao, Y.; Shum, W. W.; Her, J.-H.; Stephens, P. W.; Reiff, W. M.; Miller, J. S. Diruthenium tetraacetate monocation, $[RuII/III_2\ (O_2CMe)_4]^+$, building blocks for 3-D molecule-based magnets. *J. Am. Chem. Soc.* **2004**, *126* (37), 11630−11639.
(33) Her, J.-H.; Stephens, P. W.; Kennon, B. S.; Liu, C.; Miller, J. S. Layered (2-D) structure of $[Ru_2(O_2CMe)_4]_2[Ni(CN)_4]$ determined via rietveld refinement of synchrotron powder diffraction data. *Inorg. Chim. Acta* **2010**, *364* (1), 172−175.
(34) Cotton, F.; DeBoer, B.; LaPrade, M.; Pipal, J.; Ucko, D. The crystal and molecular structures of dichromium tetraacetate dihydrate and dirhodium tetraacetate dihydrate. *Acta Crystallogr. B: Struct. Sci. Cryst. Eng. Mater.* **1971**, *27* (8), 1664−1671.
(35) Rosi, N. L.; Kim, J.; Eddaoudi, M.; Chen, B.; O'Keeffe, M.; Yaghi, O. M. Rod packings and metal− organic frameworks constructed from rod-shaped secondary building units. *J. Am. Chem. Soc.* **2005**, *127* (5), 1504−1518.
(36) Raub, E.; Menzel, D. Die Nickel-Ruthenium-Legierungen. *International Journal of Materials Research* **1961**, *52* (12), 831−833.
(37) Kornilov, I. I. M. K.P. Phase diagram amd physical properties of Ni-Ru alloys. *Russian Metall. Mining, engl. trans.* **1964**, *1964*, 95−101.
(38) Kornilov, I. I. M. K.P. Phase diagram and physical properties of Ni-Ru alloys. *Izv. Akad. Nauk SSSR, Otd. Tekh. Nauk* **1964**, *1964*, 159−165.
(39) Hadjiivanov, K. I.; Panayotov, D. A.; Mihaylov, M. Y.; Ivanova, E. Z.; Chakarova, K. K.; Andonova, S. M.; Drenchev, N. L. Power of infrared and raman spectroscopies to characterize metal-organic frameworks and investigate their interaction with guest molecules. *Chem. Rev.* **2021**, *121* (3), 1286−1424.
(40) Liu, G.; Zhou, W.; Chen, B.; Zhang, Q.; Cui, X.; Li, B.; Lai, Z.; Chen, Y.; Zhang, Z.; Gu, L.; Zhang, H. Synthesis of RuNi alloy nanostructures composed of multilayered nanosheets for highly efficient electrocatalytic hydrogen evolution. *Nano Energy* **2019**, *66*, No. 104173.
(41) Sun, Y.; Xue, Z.; Liu, Q.; Jia, Y.; Li, Y.; Liu, K.; Lin, Y.; Liu, M.; Li, G.; Su, C. Y. Modulating electronic structure of metal-organic frameworks by introducing atomically dispersed Ru for efficient hydrogen evolution. *Nat. Commun.* **2021**, *12* (1), 1369.
(42) Geng, Z.; Liu, Y.; Kong, X.; Li, P.; Li, K.; Liu, Z.; Du, J.; Shu, M.; Si, R.; Zeng, J. Achieving a record-high yield rate of 120.9 for N_2 electrochemical reduction over Ru single-atom catalysts. *Adv. Mater.* **2018**, *30* (40), 1803498.
(43) Wang, Z. L.; Sun, K.; Henzie, J.; Hao, X.; Li, C.; Takei, T.; Kang, Y. M.; Yamauchi, Y. Spatially confined assembly of monodisperse ruthenium nanoclusters in a hierarchically ordered carbon electrode for efficient hydrogen evolution. *Angew. Chem., Int. Ed.* **2018**, *57* (20), 5848−5852.
(44) Lu, B.; Guo, L.; Wu, F.; Peng, Y.; Lu, J. E.; Smart, T. J.; Wang, N.; Finfrock, Y. Z.; Morris, D.; Zhang, P.; Li, N.; Gao, P.; Ping, Y.; Chen, S. Ruthenium atomically dispersed in carbon outperforms

platinum toward hydrogen evolution in alkaline media. *Nat. Commun.* **2019**, *10* (1), 631.
(45) Sun, F.; Wang, G.; Ding, Y.; Wang, C.; Yuan, B.; Lin, Y. NiFe-based metal−organic framework nanosheets directly supported on nickel foam acting as robust electrodes for electrochemical oxygen evolution reaction. *Adv. Energy Mater.* **2018**, *8* (21), 1800584.
(46) Lyu, S.; Wang, Y.; Qian, J.; Liu, S.; Li, Z.; Zhang, Y.; Wang, L.; Li, J. Role of residual CO molecules in OX−ZEO relay catalysis for syngas direct conversion. *ACS. Catal.* **2021**, *11* (7), 4278−4287.
(47) Genest, A.; Silvestre-Albero, J.; Li, W. Q.; Rösch, N.; Rupprechter, G. The origin of the particle-size-dependent selectivity in 1-butene isomerization and hydrogenation on Pd/Al_2O_3 catalysts. *Nat. Commun.* **2021**, *12* (1), 6098.
(48) Bouwman, J.; Fournier, M.; Sims, I. R.; Leone, S. R.; Wilson, K. R. Reaction rate and isomer-specific product branching ratios of C_2H^+ C_4H_8: 1-butene, cis-2-butene, trans-2-butene, and isobutene at 79 K. *J. Phys. Chem. A* **2013**, *117* (24), 5093−5105.
(49) Yang, D.; Xu, P.; Browning, N. D.; Gates, B. C. Tracking Rh atoms in zeolite HY: First steps of metal cluster formation and influence of metal nuclearity on catalysis of ethylene hydrogenation and ethylen e dimerization. *J. Phys. Chem. Lett.* **2016**, *7* (13), 2537−2543.
(50) Kibria Nabil, S.; McCoy, S.; Kibria, M. G. Comparative life cycle assessment of electrochemical upgrading of CO_2 to fuels and feedstocks. *Green Chem.* **2021**, *23* (2), 867−880.
(51) Müller, L. J.; Kätelhön, A.; Bringezu, S.; McCoy, S.; Suh, S.; Edwards, R.; Sick, V.; Kaiser, S.; Cuéllar-Franca, R.; El Khamlichi, A.; Lee, J. H.; von der Assen, N.; Bardow, A. The carbon footprint of the carbon feedstock CO_2. *Energy Environ. Sci.* **2020**, *13* (9), 2979−2992.
(52) Meys, R.; Kätelhön, A.; Bachmann, M.; Winter, B.; Zibunas, C.; Suh, S.; Bardow, A. Achieving net-zero greenhouse gas emission plastics by a circular carbon economy. *Science* **2021**, *374* (6563), 71−76.

https://doi.org/10.1021/jacs.4c03806
J. Am. Chem. Soc. 2024, 146, 14267−14277